Enhanced magnetic resonance signal of spin-polarized Rb atoms near surfaces of coated cells

K. F. Zhao,[1,*] M. Schaden,[2] and Z. Wu[2]
[1]*Institute of Modern Physics, Fudan University, Shanghai 200433, People's Republic of China*
[2]*Department of Physics, Rutgers University, Newark, New Jersey 07102, USA*
(Received 12 November 2009; published 21 April 2010)

We present a detailed experimental and theoretical study of edge enhancement in optically pumped Rb vapor in coated cylindrical pyrex glass cells. The Zeeman polarization of Rb atoms is produced and probed in the vicinity ($\sim 10^{-4}$ cm) of the cell surface by evanescent pump and probe beams. Spin-polarized Rb atoms diffuse throughout the cell in the presence of magnetic field gradients. In the present experiment the edge enhanced signal from the back surface of the cell is suppressed compared to that from the front surface, due to the fact that polarization is probed by the evanescent wave at the front surface only. The observed magnetic resonance line shape is reproduced quantitatively by a theoretical model and yields information about the dwell time and relaxation probability of Rb atoms on Pyrex glass surfaces coated with antirelaxation coatings.

DOI: 10.1103/PhysRevA.81.042903 PACS number(s): 34.35.+a, 75.40.Gb, 76.70.Hb, 87.57.nt

I. INTRODUCTION

The important role played by diffusion in inhomogeneous magnetic fields in nuclear magnetic resonances (NMR) was recognized as early as 1954 by Hahn [1] and has been studied extensively ever since [2]. Edge enhancement, the increased magnetic resonance signal due to the restriction of diffusion near a boundary, has also been investigated in the past decade [3−13]. So far all the studies of edge enhancement have been confined to NMR.

The effect of diffusion and magnetic field gradients on the electron paramagnetic resonances in optically pumped alkali metal vapor was studied by Skalla *et al.* and edge enhancement was not observed [14]. We have recently observed edge enhancement in optically pumped Rb vapor [15]. We also developed a detailed theory describing the edge enhancement. The theory takes into account the surface interactions of spin polarized Rb atoms. Contributions from nonlocalized and localized (edge enhanced) modes are required to explain the data [15]. The excellent signal-to-noise ratio of the present experiments allows a quantitative comparison between measured and calculated magnetic resonance line shapes, from which we deduce the average dwell time and relaxation probability of Rb atoms on coated Pyrex glass surfaces. Understanding the surface interaction of alkali metal atoms with coated glass surfaces is important in many atomic physics experiments such as magnetometry [16–18], miniature atomic devices [19], slow light [20], and quantum memory for light [21].

The present study uses evanescent waves to optically pump and probe the Zeeman polarization of Rb atoms within a distance of $\sim 10^{-4}$ cm from the surface of cylindrical Pyrex glass cells [22]. Evanescent waves have been used in several earlier studies of surface interactions of spin-polarized atoms [23–25]. In inhomogeneous magnetic fields, the Zeeman resonance line shape for slab-shaped cells depends sensitively on properties of the cell surfaces and on several experimental parameters, such as the length of the cell, the buffer gas pressure and the field gradient. Neglecting surface interactions, the line shape in such cells depends qualitatively on a dimensionless parameter $s = \frac{L}{2}(\sigma_\parallel / D)^{1/3}$, where L is the cell length, $\sigma_\parallel$ the Larmor frequency gradient due to the gradient of the longitudinal field, and D the diffusion constant [4,8,26]. When $s < 1.31$, the Rb Zeeman resonance is described by nonlocalized diffusion modes only. For $s > 1.31$, some diffusion modes become localized near the front and back surfaces in frequency space. These modes correspond to the observed edge enhancement. Some of our experimental results have already been reported [15,27]. Below we present our experiments and analysis in greater detail.

II. EXPERIMENT

A. Cell preparation

The two types of Pyrex glass cells used in the experiments are sketched in Fig. 1. The cells depicted in Fig. 1(a) have fixed length. Cells with a length greater than several millimeters are of regular cylindrical shape. Cells with a length around one millimeter are of slightly irregular shape, their central part being much thinner than the peripheral part. However, since the diameter of the central part of the cell is around 25 mm, much larger than the size of the pump and probe beams, we treat these cells as of cylindrical shape, the thickness of the cell being equal to that of the central gap of the cell. The effective length of the type of cell shown in Fig. 1(b) can be adjusted by sliding an enclosed glass prism, whose vertical surface serves as the back surface of the cell. The gap between the front cell window and the vertical prism surface can be varied from a few tens of micrometers to a few millimeters by gently tapping the stage on which the cell is mounted. We measured this gap by retro-reflection [28] to an accuracy of ± 10 μm. An advantage of using cells with adjustable length is that the cell surface properties do not change as their length is varied. The design of these cells also allows us to realize ultrathin but nevertheless uniformly coated cells of relatively large surface area.

The cells contain isotopically enriched Rb (98.3 at. % ^{87}Rb) and N_2 buffer gas at various pressures. All pressures refer to 25°C. To achieve high polarization at submicron distances from the cell surface we coat the interior cell

[*]Formerly with the Department of Physics, Rutgers University, Newark, NJ 07102.

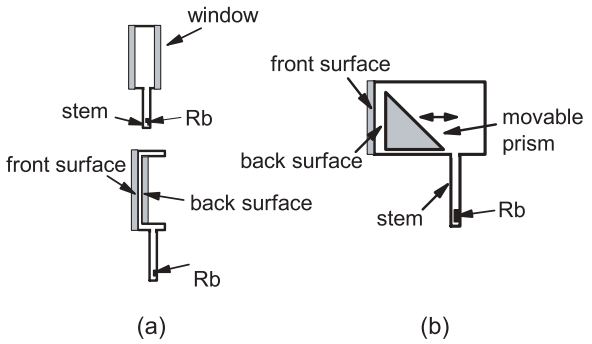

FIG. 1. The two types of Pyrex cells used in the experiments. (a) Cells of fixed length. (b) Cells whose effective length can be adjusted by sliding the enclosed prism.

surfaces with antirelaxation coatings. We use two chemicals, dichlorooctamethyltetrasiloxane (Surfasil, Pierce Chemical) and octadecyltrichlorosilane (OTS). To coat cells with Surfasil, we first wash the cells with Piranha for 1 h. After rinsing each cell thoroughly with distilled water and drying with N_2, we place a tiny drop ($\sim 2\ \mu$l) of Surfasil into the cell stem, cover the cell with aluminum foil, and heat it in an oven at 80°C for 1 h. Cells are subsequently rinsed with acetone and methanol before being put onto a manifold and baked in vacuum at 180°C overnight. The highest signal-to-noise ratio (SNR) was obtained using cells with no visible coating film. We found that in the present experiments vapor-coated cells give a better SNR than cells coated using Surfasil solution following the procedure of Ref. [29]. The reason is not entirely clear to us. The coating thickness is hard to control with vapor coating, and the coatings tend to be too thick. For coating with OTS we followed the procedures described in Ref. [30]. The OTS coatings prepared in ambient air were found to have consistently better antirelaxation quality than those prepared in a dry N_2 or Ar chamber. Presumably this is because OTS forms multilayers in ambient air, whereas it forms a monolayer in an anhydrous environment [31].

B. Magnetic fields and gradients

Edge enhancement was studied in the presence of magnetic field gradients produced by the combination of a set of three orthogonal pairs of Helmholtz coils and a round Alnico bar magnet of 0.8 cm in diameter and 20 cm in length. We use a coordinate system whose origin is at the center of the cell and whose z axis coincides with the axis of the cylindrical cell. The front and back surfaces of the cell are located, respectively, at $z = -L/2$ and $z = L/2$. The holding (longitudinal) magnetic field is along the x axis and thus parallel to the cell front and back surfaces. The bar magnet in the x-z plane is aligned parallel to the x axis and centered on the z axis. It produces a relatively large field gradient $\partial B_x/\partial z$ of the holding field B_x along the z direction. All the data reported in this article were taken with B_x increasing from the front to the back surfaces. The field gradient $\partial B_x/\partial z$ is quite uniform due to the small dimensions of the cell compared to the length of the bar magnet. The magnetic field along the y direction is negligible throughout the cell. The bar magnet also produces a transverse magnetic field B_z along the z direction, with a gradient $\partial B_z/\partial x$ along the x direction. Because $\nabla \times \mathbf{B} = 0$ for a static magnetic field, we have $\partial B_x/\partial z = \partial B_z/\partial x$. For cell lengths of less than a few millimeters we can approximate $B_x(z) = B_x(0) + z\partial B_x(0)/\partial z$. We further have $B_z(0) = 0$ so that $B_z(x) = x\partial B_z/\partial x$. To good accuracy the local Larmor frequency $\omega_L(\mathbf{x})$ is then given by [27]

$$\omega_L(\mathbf{x}) = \omega_0 + \sigma_\parallel z + x^2 \frac{\sigma_\perp^2}{2\omega_0}, \tag{1}$$

where ω_0 is the Larmor frequency at the center of the cell, $\sigma_\parallel = \gamma \partial B_x/\partial z$ is the Larmor frequency gradient associated with the gradient of the longitudinal field, and $\sigma_\perp = \gamma \partial B_z/\partial x$ that associated with the gradient of the transverse field. We have neglected terms of order $x^2 z$ in the expansion. Note that $\sigma_\parallel = \sigma_\perp$ for the present field configuration.

C. Experimental procedures

The experimental setup is sketched in Fig. 2. The cell is mounted inside a double-chamber oven. Its inner chamber is made of Peek and the outer one of Teflon. Hot air flows between the two chambers. A number of holes on the side of the inner chamber allows hot air to circulate around the cell. Care is taken so that hot air does not flow in the optical path of the laser beams, which would increase noise. To avoid condensation of Rb atoms on the cell surface, room temperature air flows through a small diameter tube to the tip of the cell (the Rb reservoir) to keep the temperature at the tip ~ 10°C lower than that of the cell body.

Zeeman polarization of the Rb vapor is produced and analyzed by right circularly polarized (σ^-) beams A and B from single-mode diode lasers operated in the free-running mode. The line width of the lasers is 45 MHz, and the diameter of the beams at half intensity is 1.0 mm. The

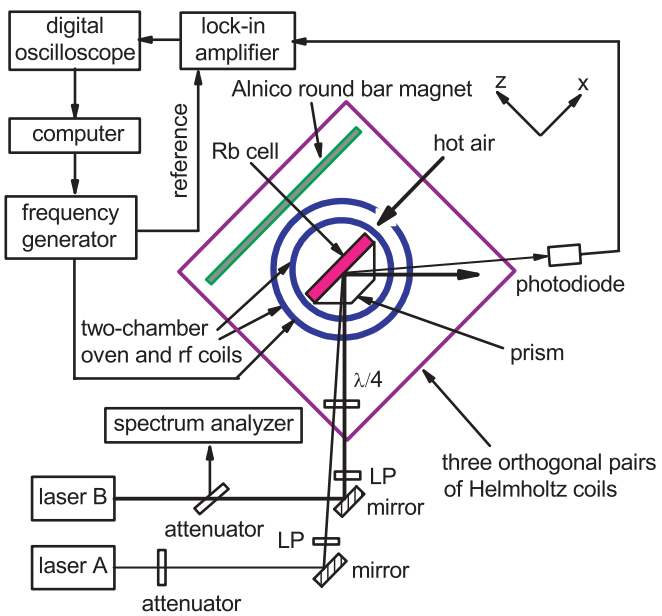

FIG. 2. (Color online) The experimental setup. Laser beams A and B are circularly polarized ($\sigma^{\pm}$) by a Glan-Thompson linear polarizer (LP) and a quarter-wave plate ($\lambda/4$).

intensities of beams A and B are, respectively, $0.5\,\mathrm{mW/cm^2}$ and $20\,\mathrm{mW/cm^2}$. The frequency of beam A is tuned to the $5^2S_{1/2}\ F=2 \rightarrow 5^2P_{1/2}\ F'=1,2$ transitions and that of beam B to the $5^2S_{1/2}\ F=1 \rightarrow 5^2P_{1/2}\ F'=1,2$ transitions. The two excited $5^2P_{1/2}\ F'=1,2$ levels were not resolved due to Doppler and collision broadening.

The two beams are incident on the front surface of the cell at the same spot $(0,0,-L/2)$ and at angles slightly larger than the critical angle. They undergo total internal reflection at the interface between the cell surface and the Rb vapor. The penetration depth of the probe beam A is 0.7 μm and that of the pump beam B approximately 2 μm, so that the two beams are spatially separate outside the cell. Both beams being in the same plane of incidence, their evanescent waves propagate in the same direction (x axis), parallel to the cell surface. A pair of radiofrequency (rf) coils wound around the Teflon oven generates an oscillating magnetic field $2B_1\cos\omega t$ along the y axis. For phase-sensitive detection, the rf field is amplitude-modulated by a square wave at $\Omega/2\pi = 200\,\mathrm{Hz}$. The intensity of the totally reflected probe beam A is monitored by a silicon photodiode, whose output is fed into a lock-in amplifier. When the radiofrequency matches the Larmor frequency of ^{87}Rb atoms, the longitudinal Zeeman polarization along the x axis is slightly diminished, causing a decrease in the intensity of the reflected beam A. We scan the radiofrequency across the Larmor frequencies of ^{87}Rb atoms, and the output of the lock-in amplifier yields a resonance curve.

III. GENERAL FEATURES OF THE ZEEMAN RESONANCE LINES

The width and central frequency of the modes that contribute to the magnetic resonance lines are the real and imaginary parts of the eigenvalues of the Torrey equation [26,32]

$$\left(D\frac{\partial^2}{\partial x^2}+D\frac{\partial^2}{\partial y^2}+D\frac{\partial^2}{\partial z^2}-i\omega(\mathbf{x})+\beta_{lmn}\right)\Psi_{lmn}(x,y,z)=0. \tag{2}$$

Using Eq. (1), Eq. (2) becomes

$$\left(D\frac{\partial^2}{\partial x^2}-ix^2\frac{\sigma_\perp^2}{2\omega_0}+D\frac{\partial^2}{\partial y^2}+D\frac{\partial^2}{\partial z^2}-i\sigma_\parallel z-i\omega_0+\beta_{lmn}\right)\times\Psi_{lmn}(x,y,z)=0. \tag{3}$$

To simplify the analysis, we assume the cell to have the shape of a square prism, with faces at $x=\pm R$, $y=\pm R$, and $z=\pm L/2$. Equation (3) in this case is separable, with eigenfunctions and eigenvalues $\Psi_{lmn}(x,y,z)=\phi_l(x)\varphi_m(y)\psi_n(z)$ and $\beta_{lmn}=\zeta_l+\epsilon_m+\alpha_n$, where ζ_l, ϵ_m, and α_n are, respectively, the eigenvalues corresponding to $\phi_l(x)$, $\varphi_m(y)$, and $\psi_n(z)$. The z mode will be referred to as the longitudinal mode, the x and y modes will be referred to as transverse modes. The diffusion in y direction is free in Eq. (3), with $\epsilon_m=D\kappa_m^2$ and $\kappa_m=(2m+1)\pi/2R$, $(m=0,1,2,\ldots)$. The eigenvalues of the Torrey equation for the x direction are $\zeta_l=(1+i)(2l+1/2)\sigma_\perp\sqrt{D/\omega_0}$ $(l=0,1,2,\ldots)$ and describe the line broadening and frequency shift due to the gradient of the transverse field [27]. Note that the eigenvalues in the x and y directions are for Dirichlet boundary conditions. Because the cell radius is much larger than the cell length, the boundary conditions for the transverse modes have little effect on the signal. However, the signal is strongly affected by the surface interactions on the front and back surfaces. The longitudinal modes $\psi_n(z)$ satisfy the equation

$$\left(D\frac{d^2}{dz^2}-i\sigma_\parallel z-i\omega_0+\alpha_n\right)\psi_n(z)=0. \tag{4}$$

The boundary conditions for $\psi_n(z)$ at $z=\pm L/2$ are [26]

$$0=\pm\frac{\partial}{\partial z}\psi_n(z)+\mu\psi_n(z)+\eta\frac{\partial^2}{\partial z^2}\psi_n(z)\Big|_{z=\pm L/2} \tag{5}$$

with

$$\mu=\sqrt{\frac{3}{2\pi}}\frac{\xi_s+i\phi_s}{\lambda}\quad\text{and}\quad\eta=\sqrt{\frac{1}{6\pi}}\tau_s\bar{v}, \tag{6}$$

where ξ_s and ϕ_s are, respectively, the average relaxation probability and average phase shift for a polarized Rb atom while it is on the surface; τ_s is its average dwell time on the surface and λ and $\bar{v}$ are, respectively, the mean free path and mean thermal velocity of Rb atoms [33]. Note that τ_s is the average time a spin polarized atom resides on the surface without its spin being relaxed. This time differs from the coherent surface interaction time τ_c, commonly measured by studying the relaxation time or magnetic decoupling of spin polarized atoms [34–37].

The eigenvalue α_n in Eq. (4) can be written as

$$\alpha_n=(D\sigma_\parallel^2)^{1/3}e_n+i\omega_0, \tag{7}$$

where e_n is the dimensionless longitudinal eigenvalue. Through the boundary conditions Eq. (5) and Eq. (6), e_n depends on surface characteristics (ξ_s, ϕ_s, and τ_s) as well as gas kinetic parameters (λ and $\bar{v}$) in a rather complicated fashion. It in general must be determined numerically [26]. In order to understand some general features of the Zeeman resonance curves, we consider the special case $\mu=\eta=0$. For such ideal coatings the spectrum $\{e_n\}$ is real except for the appearance of some complex conjugate pairs of eigenvalues when the dimensionless parameter $s=L(\sigma_\parallel/D)^{1/3}/2$ is sufficiently large [8,26]. Figure 3 shows the dependence of the two lowest pairs of eigenvalues e_0, e_1 and e_2, e_3 on s. Experimentally we change s by changing the thickness of the cell. For $s<1.31$, all the eigenvalues are real, corresponding to the fact that there are no localized modes. As s increases, e_0 and e_1 coalesce, and for $s>1.31$ they form a pair of complex conjugate eigenvalues with positive real parts, corresponding to the appearance of the first two localized modes near the front and back surfaces (edge enhancement). The eigenvalue spectrum at this point contains just one complex conjugate pair. As s increases further, e_2 and e_3 begin to coalesce, and for $s>3.06$ they form another complex conjugate pair, corresponding to the formation of a second pair of localized modes. Note that for small s, i.e., when there are only nonlocalized modes, e_n $(n>0)$ is much larger than e_0. In this case only the lowest mode e_0 contributes significantly to the signal. For large s, $\mathrm{Re}\,e_0=\mathrm{Re}\,e_1$ approach the limiting value of 0.509, half of the first real root of the derivative of the principal Airy function, while $\mathrm{Re}\,e_2=\mathrm{Re}\,e_3$ approach the limiting values of 1.625, half of the second real root of the derivative of the principal Airy function.

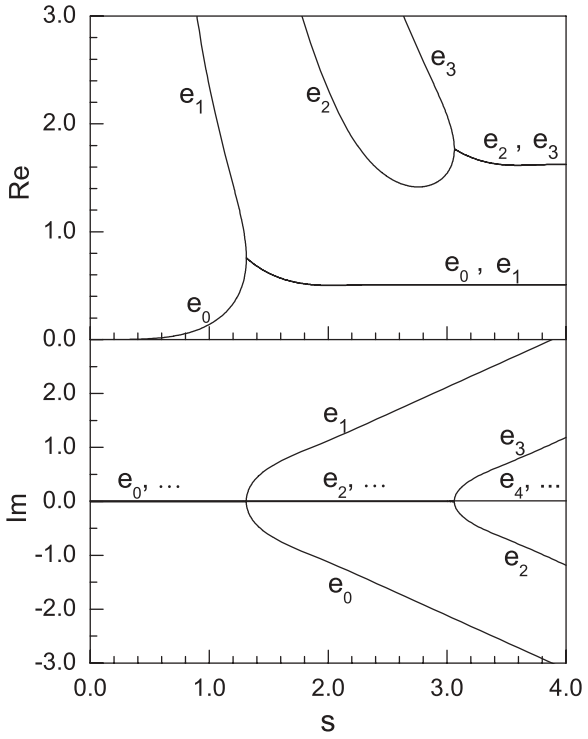

FIG. 3. The dependence of the real and imaginary parts of e_0, e_1, e_2, and e_3 on the dimensionless parameter s for ideal surfaces with $\mu = \eta = 0$.

The fact that the dimensionless eigenvalues e_n are all real for sufficiently small values of s can be understood by considering the effect of the purely imaginary interaction $V(z) = i\sigma_\parallel z$ on free diffusion in the interval $z \in [-L/2, L/2]$ to all orders in perturbation theory. For symmetric boundary conditions at both ends of the interval (for instance, Dirichlet or Neumann), the free diffusion equation is invariant under the parity transformation $P : z \to -z$ and its modes are even or odd under P. It follows that *all odd* order corrections to eigenvalues due to the odd parity perturbation $V(z)$ vanish. Corrections in even orders of perturbation theory on the other hand are *real*. Eigenvalues thus are real to all orders in the dimensionless parameter s in perturbation theory [38]. In second order the purely imaginary perturbation has precisely the opposite effect of a real one: it *increases* the lowest eigenvalue and *decreases* that of the first excited mode, that is the perturbation tends to *decrease* the gap between the first two eigenvalues. The perturbative description of the spectrum becomes inadequate for large s and certainly is no longer valid when the first two eigenvalues merge. However, this perturbative argument does show why *all* eigenvalues remain real in the presence of a (sufficiently) small non-Hermitian perturbation of this kind. Note that the invariance of $V(z)$ and thus of Eq. (4) under P combined with complex conjugation implies that eigenvalues of this diffusion either are real or come in complex conjugate pairs.

The eigenvalues e_{2n} and e_{2n+1} form a complex conjugate pair for sufficiently large values of s and the corresponding α_n approach

$$\alpha_{2n} = \frac{z_n}{2}(\sigma_\parallel^2 D)^{1/3} - i\left[\frac{L\sigma_\parallel}{2} - \frac{\sqrt{3}}{2}z_n(\sigma_\parallel^2 D)^{1/3}\right] + i\omega_0,$$
$$\alpha_{2n+1} = \frac{z_n}{2}(\sigma_\parallel^2 D)^{1/3} + i\left[\frac{L\sigma_\parallel}{2} - \frac{\sqrt{3}}{2}z_n(\sigma_\parallel^2 D)^{1/3}\right] + i\omega_0, \tag{8}$$

where $-z_n$ ($n = 0, 1, 2, \ldots$) are the real roots of the first derivative of the Airy function ($z_0 = 1.018, \ldots$). The complex eigenvalues α_{2n} and α_{2n+1} correspond to a pair of edge-enhanced modes localized near the front ($z = -L/2$) and back ($z = L/2$) surfaces in frequency space. The magnetic resonance signal is composed of a superposition of diffusion modes. The signal due to localized modes has a Lorentzian and a dispersive component [8,26].

The contributions due to the lowest pair of localized modes have a half width $\Delta\omega/2 = \Gamma_0/2 + (z_0/2)(D\sigma_\parallel^2)^{1/3} + (\sigma_\perp/2)\sqrt{D/\omega_0}$, where $\Gamma_0/2$ is the half-width of the spectral line (assumed Lorentzian) measured in the bulk in a homogeneous magnetic field. The broadening due to longitudinal and transverse field gradients are $(z_0/2)(D\sigma_\parallel^2)^{1/3}$ and $(\sigma_\perp/2)\sqrt{D/\omega_0}$, respectively. They are localized near the front (back) surface at frequencies $\omega_0 \mp \sigma_\parallel L/2 \pm (\sqrt{3}z_0/2)(D\sigma_\parallel^2)^{1/3} + (\sigma_\perp/2)\sqrt{D/\omega_0}$. Relative to the Larmor frequencies at the front and back surface, they are shifted toward the center frequency by an amount $(\sqrt{3}z_0/2)(D\sigma_\parallel^2)^{1/3} \pm (\sigma_\perp/2)\sqrt{D/\omega_0}$, where $(\sqrt{3}z_0/2)(D\sigma_\parallel^2)^{1/3}$ and $(\sigma_\perp/2)\sqrt{D/\omega_0}$ are the frequency shifts due to the longitudinal and transverse field gradients [28].

The lock-in signal is given by [27,39]

$$S(\omega, \Omega) \propto \frac{1}{R^3 D^2}\sum_{m=0}^{\infty} e^{-\kappa_m^2(r_s^2+r_p^2)/4}\sum_{l=0}^{\infty}\sum_{n=0}^{\infty}\frac{1}{2^{2l}(2l)!} \times\left[\frac{\mathcal{M}_{lmn}(0)\overline{\mathcal{M}}_{lmn}(\Omega)/a}{\frac{\Gamma_0}{2} + \beta_{lmn} + i\left(\frac{\Omega}{2} - \omega\right)} + \frac{\mathcal{M}^*_{lmn}(0)\overline{\mathcal{M}}^*_{lmn}(-\Omega)/a^*}{\frac{\Gamma_0}{2} + \beta^*_{lmn} + i\left(\frac{\Omega}{2} + \omega\right)}\right], \tag{9}$$

where the parameters r_s and r_p are, respectively, the $1/e$ radius of the pump and probe laser beams, and

$$\mathcal{M}_{lmn}(\Omega) = \int_{-L/2}^{L/2}\chi_{lm}(z; r_s, \Omega)\bar{\psi}_n(z)dz \tag{10}$$

$$\overline{\mathcal{M}}_{lmn}(\Omega) = \int_{-L/2}^{L/2}\chi_{lm}(z; r_p, \Omega)\psi_n(z)dz, \tag{11}$$

where $\chi_{lm}(z; r, \Omega)$ and $\bar{\psi}_n(z)$ are defined in Ref. [26,27].

Figure 4 shows the calculated x-quadrature component of the lock-in signal and of various longitudinal modes that contribute to a typical edge enhanced signal. Each longitudinal mode includes the contributions of all the transverse modes. There are two pairs of edge enhanced modes localized near the back and front surfaces in frequency space. Note that each individual localized contribution has a dispersive Lorentzian line shape. Due to the partial cancelation of

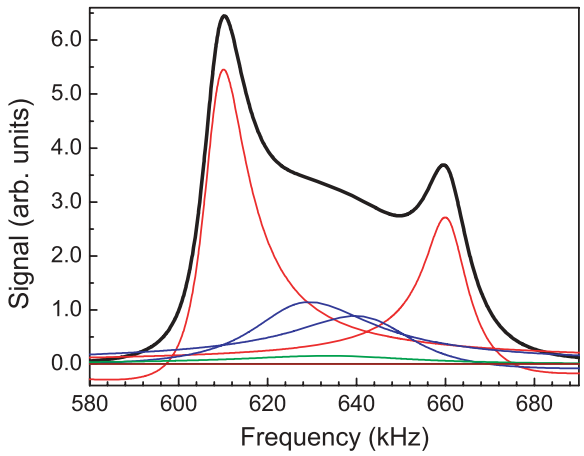

FIG. 4. (Color online) Contributions to a representative edge enhanced magnetic resonance curve. The x-quadrature component of the lock-in signal (rather than the experimentally measured $|S(\omega, \Omega)|$) is calculated numerically using Eq. (9). The parameters of this calculation are as follows: $R = 0.75$ cm, $L = 0.17$ cm, N_2 pressure = 5 Torr, cell temperature = 103°C, $\sigma_\parallel/2\pi = \sigma_\perp/2\pi = 400$ kHz/cm, $\Omega/2\pi = 0.05$ kHz, $\omega_0/2\pi = 600$ kHz, $r_s = r_p = 0.05$ cm, $T_1 = 8$ ms, $\Gamma_0/2\pi = 0.6$ kHz. Contributions to individual longitudinal modes shown in the figure include those from all transverse modes. Localized longitudinal modes correspond to complex conjugate eigenvalues and give a dispersive Lorentzian line shape. There are two pairs of edge enhanced modes (red and blue). In each pair one mode is localized near the front surface and one near the back surface in frequency space. Contributions from nonlocalized modes are much smaller and have significantly larger width. Only the two largest nonlocalized contributions are shown here (olive and wine colored curves).

Lorentzian and dispersive components, the low frequency wing of modes localized near the front surface decreases faster than a Lorentzian. Similarly the high-frequency wing of modes localized near the back surface decreases faster than a Lorentzian. Higher nonlocalized modes give only small corrections to the signal because their amplitudes are much smaller and their line width much larger.

We note that edge enhancement observed in NMR generally is symmetric, that is, localized peaks have the same height. The asymmetry in the present experiments is entirely due to the evanescent wave probing at the front surface. The peak associated with the back surface is suppressed because the polarization near the back surface has to diffuse over a larger distance before being probed. The asymmetric edge enhancement of the present experiment turns out to be rather sensitive to surface interactions [15].

Boundary condition (5) without the term proportional to the second derivative was used in earlier studies of surface interactions of spin-polarized atoms [18,40–42]. We find that the second derivative term is important and cannot be ignored in the following two interesting cases. (i) *Edge enhanced regime.* In this case the longitudinal mode $\psi_n(z) \sim A(e_n - 2isz/L)$, where A is the principal Airy function. Comparing dimensionless quantities, the relative orders of magnitude of the three terms on the right-hand side of Eq. (5) are 1, $(D/\sigma_\parallel)^{1/3}\mu$ and $(\sigma_\parallel/D)^{1/3}\eta$. Thus, when $(\sigma_\parallel/D)^{1/3}\eta \sim 1$, the term proportional to the second derivative cannot be ignored. In our experiments $\xi_s \sim 0.015$, $\tau_s \sim 1.8$ μs, $\lambda = 30$ μm, $\bar{v} = 3 \times 10^4$ cm/s, and $\sigma_\parallel/2\pi = 400$ kHz/cm for a typical Surfasil-coated cell. The relative orders of magnitude of the three terms in this case are 1, ~0.06, and ~0.40 and the third term clearly is not negligible. (ii) *Ultrathin cells.* Ignoring the longitudinal field gradient, longitudinal modes in this case are plane waves with wavenumber $k \sim 1/L$ and the relative orders of magnitude of the three terms in Eq. (5) are 1, $L\mu$, η/L. For sufficiently thin cells ($L^2 \ll \eta/\mu$), the term in the boundary condition proportional to the second derivative again is not negligible. Note that all previous experimental studies were performed in homogeneous magnetic fields, with cell dimensions of the order of centimeters [40,43] and neglecting the second derivative term was justifiable. This second derivative term in the boundary condition of the diffusion equation was first derived by considering a Poisson-distributed dwell time for polarized atoms on the surface [26], and the parameter η in Eq. (6) is proportional to the average dwell time. Note that effects of this Poisson process can be included in the boundary condition for the diffusion because it does not destroy the Markov property of the latter, i.e., it too is without memory. We have recently indirectly verified the presence of this term in the boundary condition of the diffusion equation by experimentally measuring the dwell time [44]. The dependence of the Zeeman frequency on the dwell time and the cell length for ultrathin cells in homogeneous magnetic fields can only be obtained by including this second-order derivative term in the boundary condition for the longitudinal diffusion Eq. (4) (see Sec. IV F).

IV. EXPERIMENTAL RESULTS

A. Broadening due to the longitudinal field gradient

The magnetic resonance line is subject to broadening due to the gradients of the longitudinal and transverse fields. Line broadening by inhomogeneous magnetic fields is well known and has been extensively studied in nuclear magnetic resonance experiments [1,32,45,46]. In many cases perturbation theory describes the experimental results adequately. A perturbative treatment is justified if the relaxation rate is much smaller than the differences in the decay rates of unperturbed diffusion modes. Since $R > L$ for our cylindrical cells, this condition would require,

$$L\sigma \ll \frac{D}{R^2}. \tag{12}$$

Here $\sigma = \gamma|\nabla B|$ is the Larmor frequency gradient associated with the gradient of the magnetic field. Electronic gyromagnetic ratios γ are larger than nuclear ones by two to three orders of magnitude. Thus, even though Eq. (12) is often well satisfied in NMR experiments, it is violated by several orders of magnitude in the present experiments, and both the longitudinal and transverse broadenings are nonperturbative. In this section we discuss nonperturbative line broadening due to the longitudinal field gradient. Nonperturbative line broadening due to the transverse field gradient is considered in Sec. IV B.

From Eq. (7) one sees that the nonperturbative line broadening due to the longitudinal field gradient is given by

$(\sigma_\parallel^2 D)^{1/3}\mathrm{Re}\, e_n$, where e_n depends on the cell length L and surface properties (i.e., boundary conditions). From Fig. 3 one sees that for ultrathin cells with $s = L(\sigma_\parallel/D)^{1/3}/2 \ll 1$, only the lowest mode e_0 contributes appreciably to the signal (the line width of the mode e_1 is orders of magnitude larger than that of the e_0 mode). The broadening due to the longitudinal field gradient in this case is negligible because $\mathrm{Re}\, e_0$ becomes negligibly small. This can also be seen by noting that for sufficiently thin cells ($s \ll 1$), perturbation theory is applicable, and the line broadening is given by $\sim L^4\sigma_\parallel^2/D$ [46], that is, it decreases as L^4.

Equation (10) implies that the dependence of the half width of the lowest mode on the longitudinal field gradient and surface effects is given by $\Delta\omega/2 = (D\sigma_\parallel^2)^{1/3}\mathrm{Re}\, e_0/2 +$ const., where the constant represents the line broadening due to other mechanisms. Note that the dimensionless eigenvalue e_0 is a function of s, $\tilde{\mu} = \mu(D/\sigma_\parallel)^{1/3}$ and $\tilde{\eta} = \eta(\sigma_\parallel/D)^{1/3}$ only. For sufficiently large s, the mode is localized. In this case e_0 essentially does not depend on the cell thickness L and is a function of $\tilde{\mu}$ and $\tilde{\eta}$ only. For small $\tilde{\mu}$ and $\tilde{\eta}$, the boundary conditions are approximately of Neumann type, and $\mathrm{Re}\, e_0$ is close to $z_0/2 = 0.509$, where $-z_0$ is the first root of the derivative of the principal Airy function. On the other hand, for large $\tilde{\mu}$ or $\tilde{\eta}$, the boundary conditions are close to Dirichlet type, and $\mathrm{Re}\, e_0$ approaches $x_0/2 = 1.169$, where $-x_0$ is the first root of the principal Airy function. These considerations qualitatively explain the data in Fig. 5, where the half-width $\Delta\omega/2$ of the low-frequency wing is plotted against $(\sigma_\parallel^2 D)^{1/3}$ for three OTS-coated cells (a) and three Surfasil-coated cells (b). The field gradient is varied by changing the distance between the bar magnet and the cell and is determined by measuring the peak frequency of the magnetic resonance line as a function of the distance. For OTS coatings, the slopes do not depend on the N_2 buffer gas pressure within the experimental uncertainty and are close to $z_0/2 = 0.509$. This is because both $\tilde{\mu}$ and $\tilde{\eta}$ are rather small for these coatings. The measured half-width has a systematic error of about 10% for the following reasons. (i) Even though the low-frequency wing is dominated by the lowest longitudinal mode localized near the front surface, higher modes do contribute to the signal. (ii) The lowest longitudinal mode has a Lorentzian as well as a dispersive component. For Surfasil coatings, $\tilde{\mu}$ and $\tilde{\eta}$ are no longer negligible and mixed boundary conditions must be used. The slope in this case increases with increasing N_2 density because the coefficient μ in Eq. (5) depends inversely on the mean free path [see Eq. (6)].

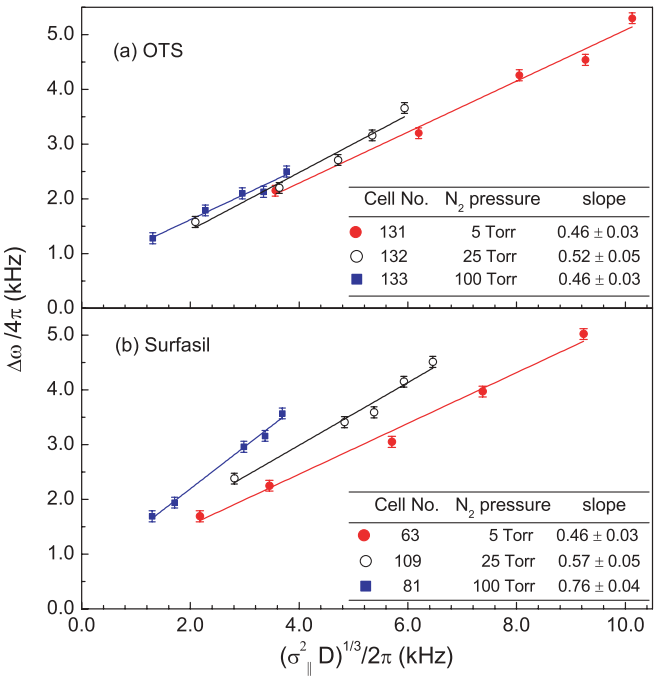

FIG. 5. (Color online) The half width at half maximum $\Delta\omega/2$ of the low-frequency side of the magnetic resonance curve versus $(\sigma^2 D)^{1/3}$ for three OTS-coated cells (a) and three Surfasil-coated cells (b). The cells are 10 mm in length and filled with N_2 gas at different pressures. The Rb density is 4.3×10^{12} cm^{-3}.

B. Line broadening due to the transverse field gradient

Line broadening due to the transverse magnetic field gradient in the present experiment is also nonperturbative. Indeed, with $R \sim 1$ cm, $\sigma/2\pi = 400$ kHz/cm, and $D = 30$ cm^2/s, condition (12) is violated by several orders of magnitude. In contrast to the perturbative case, we observed a qualitatively different dependence of line broadening on the holding field: the line broadening due to the transverse field gradient in this regime is inversely proportional to the square root of the Larmor frequency ω_0 at the center of the cell. We have reported our experimental findings and presented a simple nonperturbative theory that describes the experimental data quite well [27]. To mitigate the transverse broadening we used a relatively large holding field of about 600 kHz. The transverse broadening also depends on the probe beam size. For large probe beam diameter higher transverse modes

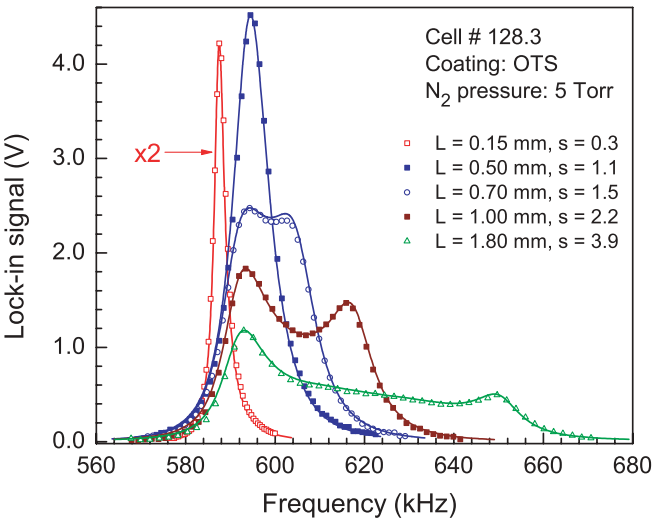

FIG. 6. (Color online) magnetic resonance curves for an OTS-coated cell (No. 128). The length of the cell is adjustable. The Larmor frequency gradient $\sigma_\parallel/2\pi$ is 400 kHz/cm. The cell is filled with 5 Torr N_2 gas and the Rb density is 4.3×10^{12} cm^{-3}. Symbols denote experimental data points, and solid lines are calculated with Eq. (9).

contribute significantly and the transverse broadening is no longer proportional to $1/\sqrt{\omega_0}$.

C. Dependence of the line shape on the cell length

Figure 6 shows representative magnetic resonance curves for an OTS-coated cell with adjustable length. The response curves calculated using Eq. (9) are also shown. The condition $s > 1.31$ for the occurrence of localized peaks when $\mu = \eta = 0$ holds to good approximation for OTS-coated cells for which $\tilde{\mu}$ and $\tilde{\eta}$ are very small. There clearly is no edge enhancement for $L = 0.15$ mm, which corresponds to $s = 0.3$. The nonlocalized modes are shifted away from the Larmor frequency ω_0 at the cell center by $(\sigma_\perp/2)\sqrt{D/\omega_0}$ due to the transverse field gradient [27]. For $L = 0.50$ mm, corresponding to $s = 1.1$, the line width is substantially broadened because of the sharp increase of $\mathrm{Re}\, e_0$ as s approaches $s = 1.31$. The first two localized modes can be resolved for $L = 0.70$ mm, corresponding to $s = 1.5$. As L increases further, the localized modes separate more ($L = 1.0$ mm). For even thicker cells, the long diffusion path from the back surface becomes more and more effective in suppressing the edge enhanced peak localized near the back surface ($L = 1.80$ mm).

The experimental arrangement is such that the position of the front surface remains fixed as the cell length is varied. Note that the observed separation between the nonlocalized peaks corresponding to $L = 0.15$ mm and $L = 0.50$ mm cells is 6.8 kHz. This compares well with their expected separation of $(\Delta L/2)\sigma_\parallel = ((0.5 - 0.15)/2)$ mm $\times$ 40 kHz/mm $= 7$ kHz due to the fact that nonlocalized peaks are always located in the middle of the cell (except for the common shift $(\sigma_\perp/2)\sqrt{D/\omega_0}$ due to the transverse field gradient that does not depend on cell length). The data in Fig. 6 also allow us to verify the frequency shift due to the longitudinal field gradient discussed in Sec. III. The frequency separation between the lowest mode localized near the front surface and any nonlocalized mode is given by $(\sqrt{3}z_0/2)(D\sigma_\parallel^2)^{1/3} - L\sigma_\parallel/2$. It does not depend on the holding field since the frequency shift due to transverse field gradients is the same for all modes to leading approximation. Consider the cells with lengths $L = 0.15$ mm and $L = 1.0$ mm in Fig. 6. For $L = 0.15$ mm all modes are nonlocalized and the peak position is at 588 kHz. For $L = 1.0$ mm the lowest mode is localized, and the front peak occurs at 593.5 kHz. For $D = 30\,\mathrm{cm^2\,s^{-1}}$, $\sigma_\parallel/2\pi = 400$ kHz/cm, and $L = 0.15$ mm, the observed frequency separation between these two peaks of 5.5 kHz is in excellent agreement with the theoretical estimate of $(\sqrt{3}z_0/2)(D\sigma_\parallel^2)^{1/3} - L\sigma_\parallel/2 = 8.06$ kHz $- 3$ kHz $=$ 5.06 kHz.

D. Dependence of the line shape on buffer gas pressures

For a given field gradient, the broadening of localized modes due to the longitudinal field gradient is proportional to the cubic root of the diffusion constant D, and D is inversely proportional to the buffer gas pressure. Shown in Fig. 7 are magnetic resonance curves for three cells of approximately the same length (10 mm). The cells contain different N_2 pressures, but have the same type of coating (OTS). The cubic root dependence of the line width on the diffusion constant is

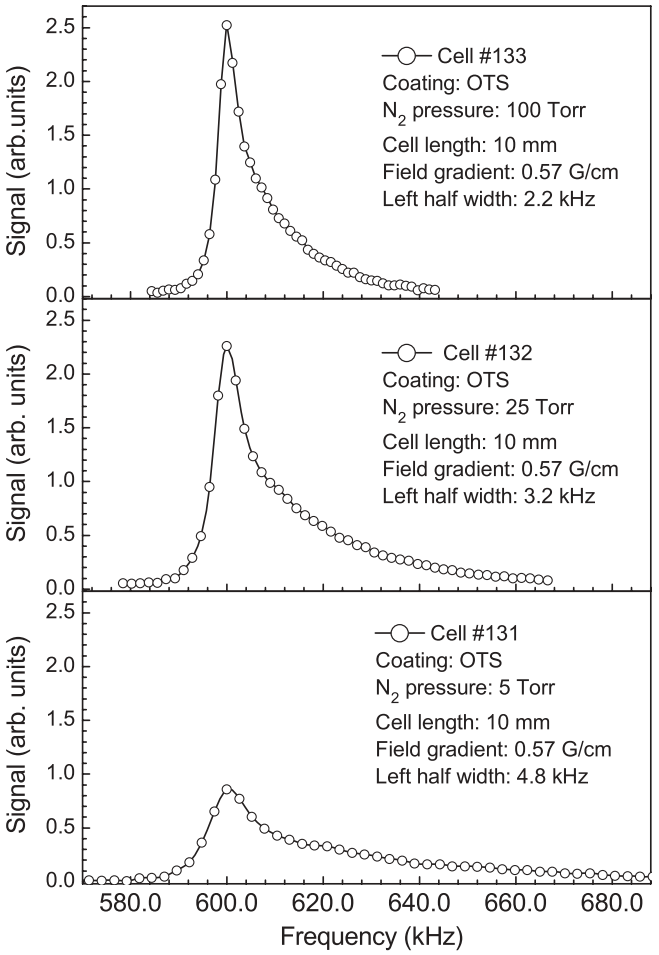

FIG. 7. The dependence of the magnetic resonance curve on the buffer gas (N_2) pressure. The OTS-coated cells are 10 mm in length and filled with N_2 gas at different pressures. The Rb density is $4.3 \times 10^{12}\,\mathrm{cm^{-3}}$.

shown in Fig. 5. One sees that as the pressure of the buffer gas N_2 increases, the line width decreases.

E. Dependence on the rf modulation frequency

Figure 8 depicts the dependence of the magnetic resonance line shape on the rf modulation frequency Ω. As Ω increases, the left half width $\Delta_{1/2}^L$ increases slightly due to the larger splitting of the side peaks [39]. The right half width $\Delta_{1/2}^R$ decreases significantly, which can be understood qualitatively as follows. The Rb atoms that contribute to the signal coherently with the rf modulation must be located at a distance l_{coherent} from the front cell surface such that

$$l_{\mathrm{coherent}} < \sqrt{2\pi D/\Omega}. \tag{13}$$

Thus an increase in the modulation frequency Ω corresponds to a smaller l_{coherent}, leading to a narrower line width since the dominant contribution to the line width is due to the longitudinal field gradient.

F. Determination of surface interaction parameters

As mentioned in Sec. III, the asymmetric edge enhancement observed in the present experiments is due to the evanescent

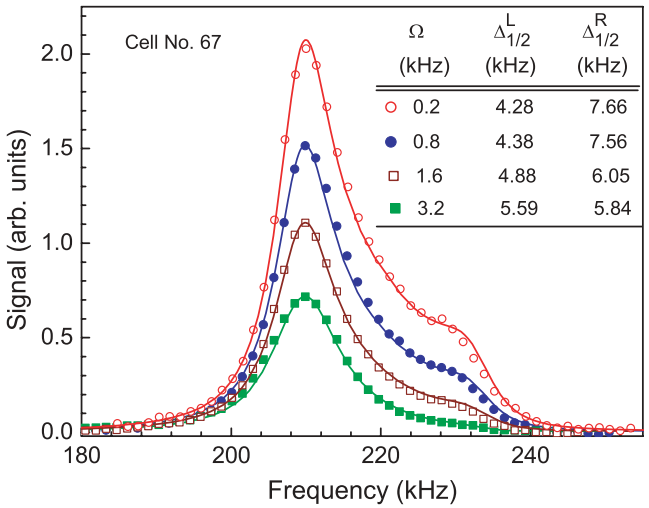

FIG. 8. (Color online) Dependence of the line shape on the rf modulation frequency. The data points were obtained using an OTS-coated cell with a (fixed) length of 0.72 mm containing ^{87}Rb and N_2 buffer gas at 15 Torr. The cell temperature is 120°C. Solid curves were calculated with the same set of parameters, changing the modulation frequency Ω only. The left and right half-widths of the left-hand peak given in the insert were found heuristically by graphical analysis of the data and are approximate.

wave probing and is rather sensitive to wall interactions of spin-polarized Rb atoms. Thus the line shape of the fully resolved edge enhanced peaks provides an interesting method to measure the surface interactions parameters of spin-polarized Rb atoms [15]. To determine the surface interaction parameters τ_s, ξ_s, and ϕ_s, we use a cell of variable length, and fit a series of magnetic resonance lines taken for a number of different cell lengths using the theory in Refs. [26,44]. A representative series of magnetic resonance lines is shown in Fig. 6. Since the surface properties for the entire series of resonance lines are the same, we use the same set of surface parameters to fit all the curves, adjusting only the length of the cell. This fitting procedure accurately determines the surface parameters τ_s and ξ_s [15].

In fitting the magnetic resonance curves it is important to take into account the broadening and shift due to the transverse field gradients in order to estimate correctly the values of ξ_s and ϕ_s, which also broaden and shift the magnetic resonance lines. The values of ξ_s and ϕ_s were overestimated in Ref. [26] because effects due to the transverse field gradient were ignored. Without taking into account the broadening due to the transverse field gradient, it is impossible to fit all the curves in a series taken for a number of different cell lengths with a single set of surface parameters although any individual resonance curve in the series may be fitted by adjusting the surface parameters.

We find that the phase shift ϕ_s caused by the surface interactions is too small to be determined reliably using this method. This is confirmed in the following experiment carried out in an OTS-coated cell whose length is adjustable between 70 and 500 μm. We study the dependence of the magnetic resonance frequency on the cell length for σ^- and σ^+ evanescent pump beams [44].

The observed Larmor frequency can be interpreted as the time-weighted average of the Larmor frequencies of a Rb atom given by

$$\omega_L^{(\pm)} = \omega_0 + \frac{\phi_s + \phi_e^{(\pm)}}{\tau_s + \tau_b}. \tag{14}$$

Here ω_0 is the Larmor frequency of a Rb atom in the bulk, ϕ_s and $\phi_e^{(\pm)}$ are, respectively, the average phase shift of a Rb atom during its dwell time τ_s on the surface and during its interaction with the evanescent $\sigma^\pm$ pump beam, and τ_b is the average time it spends in the bulk between two consecutive wall collisions. Equation (14) is valid when the spin relaxation time T_1 and the modulation period $2\pi/\Omega$ of the rf radiation are much longer than τ_s and τ_b. In the present experiment, T_1 and $2\pi/\Omega$ are of the order of 10^{-3} s, whereas τ_s and τ_b are of the order of 10^{-6} s. Time-weighted averages were previously used to estimate the frequency shift of hyperfine transitions of Rb and Cs atoms due to wall collisions [47–49]. Defining $\delta = \omega_L^{(-)} - \omega_L^{(+)}$ and $\Sigma = \omega_L^{(-)} + \omega_L^{(+)}$, we have from Eq. (14)

$$\delta = \frac{\phi_e^{(-)} - \phi_e^{(+)}}{\tau_s + \tau_b} = \frac{\phi_e^{(-)} - \phi_e^{(+)}}{\sqrt{3\pi/2}L/\bar{v} + \tau_s} \tag{15}$$

$$\Sigma = 2\omega_0 + \frac{2\phi_s}{\tau_s + \tau_b} = 2\omega_0 + \frac{\phi_s}{\sqrt{3\pi/2}L/(2\bar{v}) + \tau_s/2}. \tag{16}$$

Here we have used $\tau_b = \sqrt{3\pi/2}L/\bar{v}$ [50]. We have also used that $\phi_e^{(-)} = -\phi_e^{(+)}$ because the light shifts by $\sigma^-$and σ^+ circularly polarized light for ^{87}Rb are equal and opposite in sign. Equation (15) implies a linear relationship between the cell length L and $1/\delta$, which was used to determine the dwell time of spin polarized Rb atoms on coated glass surfaces by regression [44]. For an OTS-coated cell at temperature 103°C, we plot $\sqrt{3\pi/2}\,L/\bar{v}$ against $1/\delta$, and the intercept yields a dwell time $\tau_s = 0.56 \pm 0.03$ μs [Fig. 9(a)]. Substituting this value of τ_s into Eq. (16) and plotting Σ versus $1/[\sqrt{3\pi/2}L/(2\bar{v}) + \tau_s/2]$, the data can be fitted by a straight line [Fig. 9(b)], whose slope gives ϕ_s. From the data we find $\phi_s = -0.058 \pm 0.15$ mrad. The surface-induced phase shift ϕ_s thus is too small to be determined reliably by this experiment.

It is interesting that Eq. (14) can also be derived from the Torrey equation subject to the boundary condition (5) [26]. This derivation requires the second derivative term in the boundary condition (5). In a homogeneous magnetic field the Torrey equation Eq. (4) becomes

$$\left(D\frac{d^2}{dz^2} - i\omega_0 + \alpha_n\right)\psi_n(z) = 0. \tag{17}$$

The solutions to Eq. (17) are proportional to $\sin k_n z$ and $\cos k_n z$, corresponding to eigenvalues $\alpha_n = i\omega_0 + Dk_n^2$, where the wave numbers $k_n = 2x_n/L$, determined by the boundary conditions (5), are solutions of

$$\tan\left(x_n - n\frac{\pi}{2}\right) = \frac{L\mu}{2x_n} - \frac{2\eta}{L}x_n, \quad n = 0, 1, 2, \ldots. \tag{18}$$

To better understand the spectrum implied by Eq. (18), consider first the case where μ and η are real. As can be seen in Fig. 10, $x_0 \lesssim x_A = L\sqrt{\mu/(2L + 4\eta)}$, where x_A is the x coordinate of the intersection between the tangent to $\tan x$ at the origin, and the curve $y = \mu L/(2x) - 2\eta x/L$. For thin cells,

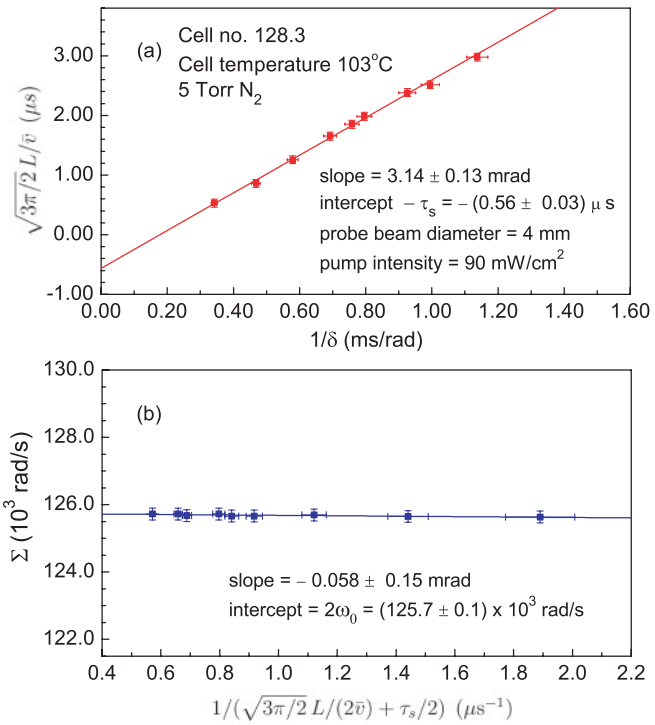

FIG. 9. (Color online) Determination of parameters characterizing the surface interaction of Rb atoms in an OTS-coated cell of variable length. Data were taken inside a two-layer magnetic shield. The holding field in units of frequency is 10 kHz. (a) A plot of $\sqrt{3\pi/2}\,L/\bar{v}$ against $1/\delta$. The negative of the intercept with the vertical axis gives the dwell time τ_s. (b) A plot of Σ as a function of $1/(\sqrt{3\pi/2}\,L/(2\bar{v}) + \tau_s/2)$. Note that the intercept $(125.7 \pm 0.1) \times 10^3$ rad/s is equal to $2\omega_0$ in Eq. (16), whence $\omega_0/2\pi = 10$ kHz, in excellent agreement with the holding magnetic field.

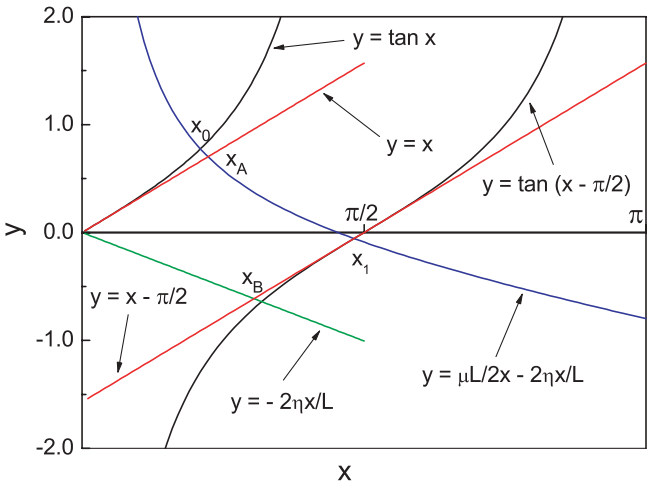

FIG. 10. (Color online) Graph illustrating the first two solutions x_0 and x_1 to Eq. (18). The solid black curves are $y = \tan(x)$ and $y = \tan(x - \pi/2) = -\cot(x)$. The tangents (red) to these curves at $x = 0$ and $x = \pi/2$ are also shown. We use unrealistic values $\mu L = 1.3$ and $\eta/L = 0.16$ to clearly resolve the bounds $x_0 < x_A$ and $x_1 > x_B$ for the intercepts with the (blue) curve $y = \mu L/(2x) - 2\eta x/L$. Thus the depicted (blue) curve is $y = 0.65/x - 0.32x$. In the present experiments μL is of order 10^{-2} and the intercept occurs too close to the origin to be seen on this plot. Note that x_A, the point where the curve $y = x$ intersects with $y = \mu L/(2x) - 2\eta x/L$ (blue) gives an upper bound for x_0. A lower bound x_B for x_1 is given by the intersection of the tangent $y = x - \pi/2$ with the line $y = -2\eta x/L$ (green) through the origin that is asymptotic to the curve $y = \mu L/(2x) - 2\eta x/L$ (blue).

x_A is quite small and an excellent approximation to x_0. For example, for $L = 0.05$ cm, $\mu \sim 0.25\,\mathrm{cm}^{-1}$, and $\eta \sim 0.01$ cm we have that $x_A = 0.08$. Note that the eigenvalue of the next solution $x_1 > L\pi/(2L + 4\eta) = \pi x_A^2/(\mu L)$ (estimated by considering the intersection of $y = -\frac{2\eta}{L}x$ with $y = x - \pi/2$). For physically reasonable surface parameters, x_1 in all our experiments is much larger than x_0 ($x_1 > 20x_0$ for the previous set of parameters). Contributions to the signal from higher modes of Eq. (17) thus are small and too broad to be relevant. For a sufficiently small imaginary part of μ we need consider only the lowest wave number $k_0 = 2x_0/L$ solution to Eq. (18). For $|x_A| \ll 1$ the lowest eigenvalue is very well approximated by

$$\alpha_0 = i\omega_0 + Dk_0^2 \simeq i\omega_0 + 4Dx_A^2/L^2 = i\omega_0 + \frac{\xi_s + i\phi_s}{\sqrt{3\pi/2}L/\bar{v} + \tau_s}. \quad (19)$$

Here Eq. (6) and $D = \lambda\bar{v}/3$ have been used to express the lowest eigenvalue in terms of the physical surface parameters and average thermal velocity. Note that in thin cells α_0 does not depend on the mean free path and therefore does not depend on the buffer gas pressure. The imaginary part of α_0 is the ensemble averaged Larmor frequency of the Rb atoms. The imaginary part of Eq. (19), which represents the shifted frequency, is identical to Eq. (14) if we include the light shift ϕ_e due to the evanescent pump beam in the surface phase shift ϕ_s, i.e., replace ϕ_s in Eq. (19) by $\phi_s + \phi_e$.

Note that in deriving $\omega_L^{(\pm)}$ in Eq. (14) one has to average over the average Larmor frequencies of the individual atoms in the ensemble. The average Larmor frequency of an individual atom is also given by Eq. (14) with τ_s and τ_b denoting the average dwell and bulk times of that atom. In obtaining Eq. (14) the width of the distribution of the individual averages for the atoms in the ensemble is neglected and τ_s and τ_b are replaced by ensemble averaged quantities. As we have now seen, this approximation is justified if higher modes of the Torrey equation can be ignored. The contribution from the lowest mode of Eq. (17) already reproduces Eq. (14). However, contrary to Eq. (14), Eq. (17) with boundary conditions (5) continues to describe the observed Larmor frequency even when higher modes become significant and Eq. (19) is no longer sufficient in describing the response. In this case the width of the ensemble distribution cannot be ignored and Eq. (14) does not give the correct frequency shift.

V. CONCLUSION

We observed edge enhancement in the magnetic resonance response of optically pumped Rb vapor and studied the line shape both experimentally and theoretically. The experiments were performed with coated cells in the presence of magnetic field gradients. The excellent signal-to-noise ratio allowed a detailed study of the line shape, including its dependence on cell length, field gradient, buffer gas pressure, rf modulation

frequency and surface interactions. Edge enhancement in optically pumped Rb vapor is more sensitive to surface depolarization effects than edge enhancement in NMR because the surface interaction of spin polarized electrons is much stronger than that of spin-polarized nuclei. A unique feature of our experiments is that Rb atoms are optically pumped and probed in the vicinity ($\sim 10^{-4}$ cm) of the cell surface by evanescent waves. The evanescent wave probing at the front surface of the cell leads to an asymmetric edge enhancement, the localized peak near the back surface being suppressed due to the longer diffusion path back to the front surface, where the polarization of the Rb atoms is probed. A systematic study of the dependence of the line shape on the cell length for cells whose length could be varied from several tens to several hundred microns allowed us to extract the depolarization probability, average surface phase shift and average dwell time for Rb atoms interacting with the coated surface. For a cell surface temperature of 103°C we found surface depolarization probabilities of $\xi_s \sim 0.015(4)$ and average surface dwell times of $\tau_s \sim 1.8(2)\mu$s for Surfasil-coated cells, whereas the corresponding values for OTS-coated cells were $\xi_s \sim 0.0016(5)$ and $\tau_s \sim 0.53(3)\mu$s. Although average dwell times and surface depolarization probabilities can be determined reliably in this manner, we obtain only an upper bound for the average intrinsic phase shift due to surface interactions of $|\phi_s| < 0.2$ mrad for both OTS and Surfasil coatings.

We developed a detailed theoretical understanding of edge enhancement in optically pumped Rb vapor. The theory quantitatively reproduces the resonance lines for all the experimental conditions we investigated. In contrast to previous theoretical studies of edge enhancement, the theory we developed includes surface interactions. Assuming a Poisson process for the dwell times, their effect on the magnetization is described by a term in the boundary conditions for the Torrey equation governing the (transverse) magnetization. The term depends on the second derivative of the magnetization. We confirmed the presence of this term by studying the dependence of the Zeeman frequency shift in thin cells whose length was adjustable. We also show that this term does not depend on the mean free path. For our experimental conditions, surface effects in very thin cells are mainly due to the lowest mode of the Torrey equation. In this approximation, the frequency shift by surface interactions is given by the time weighted average used in earlier studies.

ACKNOWLEDGMENTS

The experiments described in this article were performed at Rutgers University. Z.W. acknowledges the support of the ONR, M.S. the support of the NSF, and K.F.Z. the support of the startup funds at Fudan University. We thank Jerry Weido for making our specially designed cells.

[1] E. L. Hahn, Phys. Rev. **80**, 580 (1950).
[2] P. T. Callaghan, *Principles of Nuclear Magnetic Resonance Microscopy* (Oxford University Press, Oxford, 1991), and references therein.
[3] D. Grebenkov, Rev. Mod. Phys. **79**, 1077 (2007).
[4] S. D. Stoller, W. Happer, and F. J. Dyson, Phys. Rev. A **44**, 7459 (1991).
[5] B. Pütz, D. Barsky, and K. Schulten, Chem. Phys. Lett. **183**, 391 (1991); J. Magn. Reson. (1969–1992) **97**, 27 (1992).
[6] P. T. Callaghan *et al.*, J. Magn. Reson. A **101**, 347 (1993).
[7] T. de Swiet and P. Sen, J. Chem. Phys. **100**, 5597 (1994).
[8] T. de Swiet, J. Magn. Reson. **109**, 12 (1995).
[9] B. Saam, N. Drukker, and W. Happer, Chem. Phys. Lett. **263**, 481 (1996).
[10] Y. Q. Song, B. M. Goodson, B. Sheridan, T. M. de Swiet, and A. Pines, J. Chem. Phys. **108**, 6233 (1998).
[11] C. H. Tseng, G. P. Wong, V. R. Pomeroy, R. W. Mair, D. P. Hinton, D. Hoffmann, R. E. Stoner, F. W. Hersman, D. G. Cory, and R. L. Walsworth, Phys. Rev. Lett. **81**, 3785 (1998).
[12] M. V. Romalis and W. Happer, Phys. Rev. A **60**, 1385 (1999).
[13] S. Axelrod and P. Sen, J. Chem. Phys. **114**, 6878 (2001).
[14] J. Skalla, G. Wäckerle, and M. Mehring, Opt. Comm. **143**, 209 (1997).
[15] K. F. Zhao, M. Schaden, and Z. Wu, Phys. Rev. A **78**, 034901 (2008).
[16] D. Budker, V. Yashchuk, and M. Zolotorev, Phys. Rev. Lett. **81**, 5788 (1998).
[17] M. V. Balabas, D. Budker *et al.*, J. Opt. Soc. Am. B **23**, 1001 (2006).
[18] S. J. Seltzer and M. V. Romalis, J. Appl. Phys. **106**, 114905 (2009).
[19] P. D. D. Schwindt, B. Lindseth, S. Knappe, V. Shah, J. Kitching, and L. Liew, Appl. Phys. Lett. **90**, 081102 (2007); S. Knappe, V. Shah, P. D. D. Schwindt, L. Hollberg, J. Kitching, L. Liew, and J. Moreland, *ibid.* **85**, 1460 (2004).
[20] Y. Xiao, M. Klein, M. Hohensee, L. Jiang, D. F. Phillips, M. D. Lukin, and R. L. Walsworth, Phys. Rev. Lett. **101**, 043601 (2008).
[21] B. Julsgaard1, J. Sherson, J. I. Cirac, J. Fiurášek and E. S. Polzik, Nature **432**, 482 (2004).
[22] K. F. Zhao and Z. Wu, Appl. Phys. Lett. **89**, 261113 (2006).
[23] S. Grafström and D. Suter, Phys. Rev. A **54**, 2169 (1996).
[24] K. Zhao and Z. Wu, Phys. Rev. A **71**, 012902 (2005); Phys. Rev. Lett. **91**, 113003 (2003).
[25] K. Zhao and Z. Wu, Phys. Rev. A **70**, 010901(R) (2004).
[26] M. Schaden, K. F. Zhao, and Z. Wu, Phys. Rev. A **76**, 062502 (2007); **77**, 049903(E) (2008).
[27] K. F. Zhao, M. Schaden, and Z. Wu, Phys. Rev. A **78**, 013418 (2008).
[28] P. J. Thomas, R. Mani, and N. Khalil, Rev. Sci. Instrum. **70**, 2225 (1999).
[29] X. Zeng, Z. Wu, T. Call, E. Miron, D. Schreiber, and W. Happer, Phys. Rev. **31**, 260 (1985).
[30] M. S. Rosen, T. E. Chupp, K. P. Coulter, R. C. Welsh, and S. D. Swanson, Rev. Sci. Instrum. **70**, 1546 (1999).
[31] Y. W. Yi, H. G. Robinson, S. Knappe, J. E. Maclennan, C. D. Jones, C. Zhu, N. A. Clark, and J. Kitching, J. Appl. Phys. **104**, 023534 (2008).
[32] H. C. Torrey, Phys. Rev. **104**, 563 (1956).

[33] Note that the values of μ and η defined in Eq. (6) are smaller than those defined in Ref. [26] by a factor $\sqrt{\frac{\pi}{6}}$. The reason for this discrepancy is that the boundary conditions in Ref. [26] were derived using a simple hopping model, whereas the derivation of Eq. (5) is based on gas kinetic theory.

[34] M. A. Bouchiat and J. Brossel, Phys. Rev. **147**, 41 (1966).

[35] B. Driehuys, G. D. Cates, and W. Happer, Phys. Rev. Lett. **74**, 4943 (1995).

[36] J. Camparo, J. Chem. Phys. **86**, 1533 (1987).

[37] W. Nagengast, A. Nass, C. Grosshauser, K. Rith, and F. Schmidt, J. Appl. Phys. **83**, 5626 (1998).

[38] Equation (4) belongs to a class of differential equations considered in Ref. [51]. The spectrum of this operator is real only in a bounded space and for a sufficiently small (but finite) perturbation. For $L \to \infty$ also the parameter $s \to \infty$, no matter how small the perturbation. In this limit *all* eigenmodes become localized with corresponding complex eigenvalues—in complete agreement with the findings for infinite space in Ref. [51].

[39] For square-wave modulation used in the experiment the signal is proportional to $|S(\omega + \Omega/2, \Omega) + S(\omega - \Omega/2, \Omega)|$ and therefore consists of a peak at ω and two side peaks at $\omega - \Omega$ and $\omega + \Omega$.

[40] F. Masnou-Seeuws and M. A. Bouchiat, J. Phys. **28**, 406 (1967).

[41] Z. Wu, S. Schaefer, G. D. Cates and W. Happer, Phys. Rev. A **37**, 1161 (1988).

[42] S. J. Seltzer, D. M. Rampulla, S. Rivillon-Amy, Y. J. Chabal, S. L. Bernasek, and M. V. Romalis, J. Appl. Phys. **104**, 103116 (2008).

[43] Z. Wu, W. Happer, M. Kitano, and J. Daniels, Phys. Rev. A **42**, 2774 (1990).

[44] K. F. Zhao, M. Schaden, and Z. Wu, Phys. Rev. Lett. **103**, 073201 (2009)

[45] R. L. Gamblin and T. R. Carver, Phys. Rev. **138**, A946 (1965); F. D. Colegrove, L. D. Schearer and G. K. Walters, *ibid.* **132**, 2561 (1963); L. D. Schearer and G. K. Walters, *ibid.* **139**, A1398 (1965); D. D. McGregor, Phys. Rev. A **41**, 2631 (1990); S. Pustelny, D. F. Jackson Kimball, S. M. Rochester, V. V. Yashchuk, and D. Budker, *ibid.* **74**, 063406 (2006).

[46] G. D. Cates, S. R. Schaefer, and W. Happer, Phys. Rev. A **37**, 2877 (1988); G. D. Cates, D. J. White, T. R. Chien, S. R. Schaefer, and W. Happer, *ibid.* **38**, 5092 (1988).

[47] H. M. Goldenberg, D. Kleppner, and N. F. Ramsey, Phys. Rev. **123**, 530 (1961).

[48] R. G. Brewer, J. Chem. Phys. **38**, 3015 (1963).

[49] J. Vanier, J. F. Simard, and J. S. Boulanger, Phys. Rev. A **9**, 1031 (1974).

[50] Consider a slab-shaped cell with a cell thickness L and front and back surface area A. Assume $L \ll \sqrt{A}$. The percentage of Rb atoms hitting the front surface during time interval dt is

$$\frac{dN(t)}{N_0} = \frac{dt}{L}\int_0^\infty v_x \sqrt{\frac{m}{2\pi kT}} \exp\left(-\frac{mv_x^2}{2kT}\right) dv_x = \frac{\bar{v}}{L}\sqrt{\frac{1}{6\pi}}dt, \tag{20}$$

where $N(t)$ is the number of Rb atoms that have hit the front surface between time $t = 0$ and t, N_0 the total number of Rb atoms, and $\bar{v} = \sqrt{3kT/m}$ is the mean velocity of Rb atoms. The thermal Maxwell distribution of v_x is used in Eq. (20). The fraction of Rb atoms hitting the front or back surfaces during dt is given by

$$\frac{dN(t)}{N_0} = 2\frac{\bar{v}}{L}\sqrt{\frac{1}{6\pi}}dt = \frac{dt}{\tau_b}, \tag{21}$$

where

$$\tau_b = \frac{L}{\bar{v}}\sqrt{\frac{3\pi}{2}}. \tag{22}$$

From Eq. (21) we find $N(\tau_b) = N_0$, that is, on average a Rb atom will hit the front or back surfaces once every τ_b time interval or the average time a Rb atom stays in the bulk between two consecutive wall collisions is τ_b.

[51] C. M. Bender and S. Boettcher, Phys. Rev. Lett. **80**, 5243 (1998).